

## Partial liquid metal dealloying to synthesize nickel-containing porous and composite ferrous and high-entropy alloys

Takeshi Wada <sup>1✉</sup>, Pierre-Antoine Geslin<sup>1,2</sup>, Daixu Wei<sup>1</sup> & Hidemi Kato <sup>1</sup>

Liquid metal dealloying is a promising technique to produce bicontinuous porous metals with high specific surface areas. This processing technique relies on the selective dissolution of a component from a precursor alloy into a metal bath while the remaining insoluble component self-assembles into an interconnected structure. However, it has not been applied to produce nickel-containing porous metals because of the lack of a suitable metallic bath. Here we show that nickel-containing porous metals can be produced by partial liquid metal dealloying. The amount of soluble component in the resulting microstructure can be tuned by carefully choosing the bath element so that the ligaments of desired composition equilibrate with the metal bath. We demonstrate this partial liquid dealloying concept using magnesium and bismuth baths and rationalize the results through thermodynamics calculations. Furthermore, we apply this technique to produce porous nickel-containing stainless steel and high-entropy alloy.

<sup>1</sup>Institute for Materials Research, Tohoku University, Sendai 980-8577, Japan. <sup>2</sup>University of Lyon, CNRS, INSA Lyon, UCBL. MATEIS, UMR 5510, 69100 Villeurbanne, France. ✉email: [takeshi.wada.d7@tohoku.ac.jp](mailto:takeshi.wada.d7@tohoku.ac.jp)

Nanoporous metals with bicontinuous microstructures are attracting increasing attention owing to their outstanding performance as electrodes, catalysts, and sensors<sup>1–7</sup>. This can be attributed to their unique characteristics: high porosity and specific surface areas, permeability to fluids, and a freestanding nature that facilitates easy manipulation. Such nanoporous materials are prepared by the selective removal of a component from a solid alloy, also known as dealloying<sup>1–3</sup>. Dealloying was initially introduced as an electrochemical process whereby the less-noble component of the precursor selectively ionizes and dissolves into an aqueous solution, whereas the remaining noble component self-organizes into a three-dimensional nanoporous structure<sup>8–10</sup>. However, this electrochemical technique is only applicable to elaborate nanoporous structures comprising noble metals such as Au<sup>1</sup>, Pt<sup>11</sup>, and Cu<sup>7,12</sup>.

In the past decade, the concept of dealloying has been extended to other processes that rely on the selective dissolution of a component of an alloy into a surrounding medium. Organic solvents<sup>13</sup>, molten salts<sup>14</sup>, and liquid metals<sup>15</sup> have been used to promote this selective dissolution. Solid-state<sup>16,17</sup> and vapor-phase<sup>18</sup> dealloying techniques have also been introduced. These new processes do not rely on the electrochemical properties of the alloy elements, and are therefore applicable to a larger variety of metals and semiconductors.

Among these techniques, liquid metal dealloying (LMD)<sup>15</sup> has emerged as a versatile method that can be used to produce various porous and composite metals. In LMD, the selective dissolution is driven by the mixing enthalpy  $\Delta H_{\text{mix}}$  between species rather than the difference between their electrochemical potentials. Let us consider a generic A-B precursor alloy immersed in a liquid metal C (here, A, B, and C denote single or multiple components). Selective dissolution of B and formation of nanoporous A, as schematically shown in Fig. 1a, occurs if A is

immiscible in C ( $\Delta H_{\text{mix}}^{\text{A-C}}$  large) and B is miscible in C ( $\Delta H_{\text{mix}}^{\text{B-C}} \lesssim 0$ ). The development of connected microstructures in LMD originates from an interfacial spinodal decomposition (promoted by the large  $\Delta H_{\text{mix}}^{\text{A-C}}$ ) coupled with a diffusion-limited growth mechanism<sup>19</sup>. Using LMD, porous and composite materials comprising Ti<sup>15</sup> and its alloys<sup>20</sup>, ferrous alloys<sup>21</sup>, Nb<sup>22</sup>, Mo<sup>23</sup>, Ta<sup>3,19,24</sup>, Si<sup>25</sup>, carbon<sup>26,27</sup>, or high-entropy alloys (HEAs)<sup>28</sup> have been successfully fabricated. These materials present interesting mechanical properties<sup>24,29</sup> and advantageous functional properties for battery electrodes<sup>25</sup>, electrolytic capacitors<sup>22</sup>, soft magnetic material<sup>30</sup>, and catalytic materials<sup>23</sup>. Recently, the LMD method is combined with the additive manufacturing process for the scalable and tunable synthesis of composite materials with the uniform features throughout the entire bulk<sup>31</sup>.

In the previous LMD studies, Mg<sup>15,20–22,28–30</sup>, Cu<sup>3,19,24,31</sup> and Bi<sup>25,26</sup> are commonly used in the metallic baths owing to their availability and because they can be easily etched away in acidic solution to obtain nanoporous samples of the desired elements. Also, using low melting point metals such as Mg and Bi is beneficial because the temperature of the dealloying experiment can be significantly lower than the melting temperature of the precursor alloy, which limits surface diffusion and results in finer ligament microstructures<sup>32</sup>. However, the high miscibility of Ni in Mg and Cu liquids precludes the application of LMD to the production of Ni-containing porous alloys. It should be noted that porous Ni-Cr alloys have been produced through LMD using an Ag liquid bath<sup>33</sup>, but Ag remains far from an ideal choice for a metallic bath owing to its cost. However, alloys containing Ni are widely used as structural and functional materials in a large range of applications; austenitic steels and Ni-based super-alloys are notable examples of alloys with excellent mechanical properties that are exploited by modern industry. As functional materials, Ni alloys are also widely used for their shape-memory and catalytic properties<sup>34–36</sup>.

Therefore, it appears highly desirable to establish a liquid metal dealloying method that facilitates the production of Ni-containing porous alloys; such was the focus of the present work. The basic idea developed throughout this article consists in adding an amount of B (Ni) to the liquid bath such that only a fraction of B dissolves from the A-B precursor, as schematically shown in Fig. 1b. The dealloying naturally stops when an equilibrium is reached between solid and liquid phases, i.e. when the composition of the ligaments reaches the desired tie-line on the phase diagram. Practically, one searches for a tie-line in a ternary phase diagram connecting a desired composition  $A_{1-x}B_x$  solid with a  $B_yC_{1-y}$  melt. In such a system, by immersing a precursor of  $A_{1-x'}B_{x'}$  ( $x' > x$ ) in a  $B_yC_{1-y}$  bath, the content of B in the precursor decreases until the composition of the solid reaches  $A_{1-x}B_x$  to achieve thermodynamic equilibrium with the liquid. This is referred to as partial liquid metal dealloying (PLMD) in the following. Note that in LMD experiments, the size of the precursor sample is small compared to the volume of the liquid bath. Thus, upon dealloying, the content of B in the bath does not change significantly and does not reach the solubility limit of B in C. The present study builds on the powerful concept of tuning the composition of the liquid bath to control the properties of the dealloyed microstructure. In a recent contribution, Lai et al.<sup>37</sup> showed numerically and experimentally that modifying the liquid bath composition to limit the leakage of immiscible (A) element into the melt facilitates control of the topology of the resulting microstructures, which is conceptually different from our work that aims at controlling the composition of miscible (B) element in resulting solid ligaments. In another numerical study, Lai et al.<sup>38</sup> described how a threshold amount of B in the melt can also change the resulting morphologies, inhibiting the dealloying reaction and promoting a planar dissolution regime.

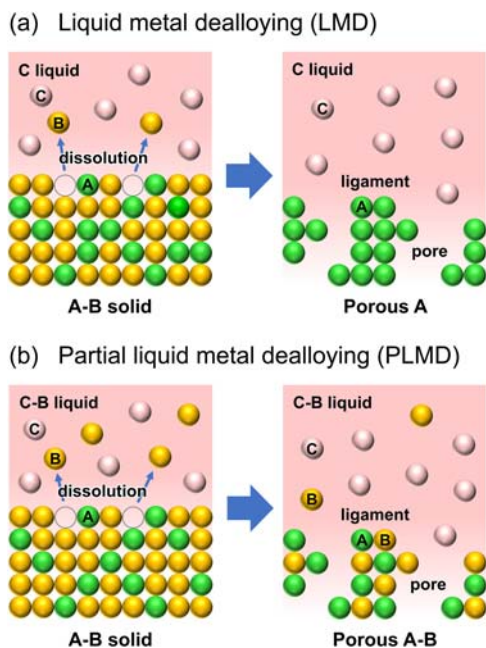


**Fig. 1** Schematic illustrations for liquid metal dealloying (LMD) and partial liquid metal dealloying (PLMD). **a** In conventional liquid metal dealloying, when the A-B solid precursor is immersed in the C metallic bath, most of the B element in the precursor solid dissolves to form a porous metal consisting of almost pure A. **b** In partial liquid metal dealloying, when the A-B solid precursor is immersed in the C-B alloy bath, a part of B element in the precursor solid dissolves to form a porous metal composed of A and B elements.

In the present work, we aimed to achieve the PLMD of Fe-Ni-based precursor alloys, and to produce porous alloys containing a controlled amount of Ni. After presenting the thermodynamical description of the PLMD strategy, we focused on Mg and Bi baths to demonstrate how adding Ni to the liquid metal facilitates the control of the residual Ni content in the solid ligaments. These experimental findings were also rationalized by Calphad calculations. We used this PLMD technique to produce porous and composite Ni-containing alloys, including Fe-Ni binary alloys, an austenitic stainless steel close to the 316L grade, and a high entropy alloy of face-centered cubic (FCC) structure.

## Results

### Thermodynamic description of the concept of partial liquid metal dealloying

**Nomenclature.**  $x_B^{(l)}$ : Mole fraction of B component in liquid phase

$x_B^{(s)}$ : Mole fraction of B component in solid phase

$G^{(l)}$ : Molar Gibbs free energy of liquid phase as a function of  $x_B^{(l)}$

$G^{(s)}$ : Molar Gibbs free energy of solid phase as a function of  $x_B^{(s)}$

$G_i^{(l)}$ : Molar Gibbs free energy of pure i component in liquid state

$G_i^{(s)}$ : Molar Gibbs free energy of pure i component in solid state

$\Omega_{ij}^{(l)}$ : Interaction parameter between i and j components in liquid phase

$\Omega_{ij}^{(s)}$ : Interaction parameter between i and j components in solid phase

R: Gas constant

T: Absolute temperature

To introduce the rationale behind the concept of PLMD, we first propose a simple thermodynamic description of the dealloying process based on regular solution models for the A-B solid and the B-C liquid phases. Assuming that A does not dissolve in the liquid, and that C does not diffuse in the solid phase because of the immiscibility of A and C, the molar Gibbs free energies of both liquid and solid phases can be written as functions of their B contents<sup>39</sup>:

$$G^{(l)} = G_B^{(l)} x_B^{(l)} + G_C^{(l)} (1 - x_B^{(l)}) + \Omega_{BC}^{(l)} x_B^{(l)} (1 - x_B^{(l)}) + RT \left( x_B^{(l)} \ln(x_B^{(l)}) + (1 - x_B^{(l)}) \ln(1 - x_B^{(l)}) \right) \quad (1)$$

$$G^{(s)} = G_B^{(s)} x_B^{(s)} + G_A^{(s)} (1 - x_B^{(s)}) + \Omega_{AB}^{(s)} x_B^{(s)} (1 - x_B^{(s)}) + RT \left( x_B^{(s)} \ln(x_B^{(s)}) + (1 - x_B^{(s)}) \ln(1 - x_B^{(s)}) \right) \quad (2)$$

Upon immersion of the precursor in the bath, the system is initially out of equilibrium, which promotes the selective dissolution of B in the liquid and the LMD reaction (as sketched in Fig. 1a, b). We will assume that the liquid bath is sufficiently large that the dissolution of B does not significantly affect the composition of the bath.

While the composition of the liquid does not change, the content of B in the solid decreases progressively as it dissolves selectively in the liquid. Eventually, the system reaches a thermodynamic equilibrium where the solid ligaments are in equilibrium with the liquid phase. This equilibrium can be written by equating the chemical potentials of B in both phases, which yields a relation between the compositions of the solid and liquid phases:

$$\Omega_{AB}^{(s)} \left(1 - x_B^{(s)}\right)^2 + RT \ln(x_B^{(s)}) = \Omega_{BC}^{(l)} \left(1 - x_B^{(l)}\right)^2 + RT \ln(x_B^{(l)}) + \left(G_B^{(l)} - G_B^{(s)}\right) \quad (3)$$

Therefore, the composition of the liquid bath controls the amount of B remaining in the ligaments, and this dependence is a function of the interaction parameters  $\Omega_{BC}^{(l)}$  and  $\Omega_{AB}^{(s)}$ . To illustrate

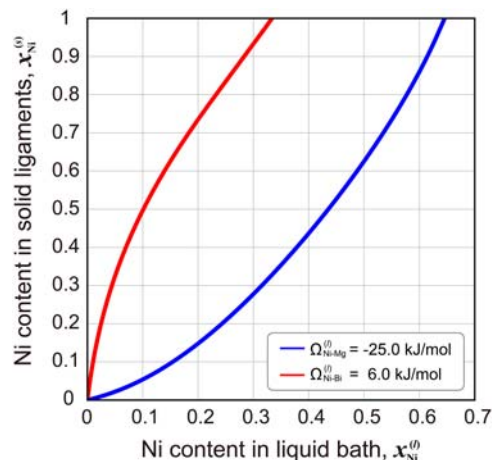


**Fig. 2 Equilibrium composition of Ni in solid ligament as a function of liquid bath composition predicted by the regular solution model.**

Equilibrium composition of solid ligament and liquid bath for the typical dealloying reactions of Fe-Ni precursor dealloyed in Mg-based or Bi-based bath at 1023 K was estimated using Eq. (3). We used realistic parameters,  $G_{Ni}^{(l)} - G_{Ni}^{(s)} = 6.8 \text{ kJ mol}^{-1}$ ,  $\Omega_{Fe-Ni}^{(s)} = -8.7 \text{ kJ mol}^{-1}$ ,  $\Omega_{Ni-Mg}^{(l)} = -25 \text{ kJ mol}^{-1}$ , and  $\Omega_{Ni-Bi}^{(l)} = 6 \text{ kJ mol}^{-1}$ , reported in the literatures<sup>40,41</sup>. Blue and red curves represent equilibrium composition of solid ligament in Mg-based (blue) or Bi-based (red) bath, respectively.

this relation, we consider the typical reaction of a Fe-Ni (=A-B) precursor dealloyed in two different baths (C = Mg, Bi) at 1023 K. We consider realistic parameters:  $G_{Ni}^{(l)} - G_{Ni}^{(s)} = 6.8 \text{ kJ mol}^{-1}$  and  $\Omega_{Fe-Ni}^{(s)} = -8.7 \text{ kJ mol}^{-1}$  for the Fe-Ni system<sup>40</sup>, and  $\Omega_{Ni-Mg}^{(l)} = -25 \text{ kJ mol}^{-1}$  and  $\Omega_{Ni-Bi}^{(l)} = 6 \text{ kJ mol}^{-1}$  for the liquid bath<sup>40,41</sup>. Figure 2 displays the equilibrium composition of Ni in the solid ligaments as a function of the liquid bath composition obtained from the numerical resolution of Eq. (3). It reveals that adding Ni to the liquid bath enables the retention of Ni in the solid ligaments, but the behaviors of the Mg and Bi baths appear very different. In the case of the Mg bath,  $\Omega_{Ni-Mg}^{(l)} < \Omega_{Fe-Ni}^{(s)}$  promotes the dissolution of Ni in the liquid bath; even with significant amounts of Ni in the liquid, Ni still dissolves in the liquid to minimize the free energy of the system. The situation is different for a Bi bath in which  $\Omega_{Ni-Bi}^{(l)} > \Omega_{Fe-Ni}^{(s)}$ , resulting in the concave red curve in Fig. 2; the residual amount of Ni in the solid is very sensitive to the Ni content of the liquid. The regular solution model presented here qualitatively shows that changing the composition of the melt enables the control of the residual amount of B (Ni) in the ligaments. This consists in the concept of the PLMD, which will be harnessed in the following.

**Liquid metal dealloying of a Fe-Ni precursor in various Mg-Ni alloy baths.** We investigated the dealloying reaction of a Fe-Ni precursor alloy immersed in Mg baths containing various amounts of Ni. The dealloying reaction was possible because Fe is strongly immiscible with a Mg melt (the solubility is 0.02 atomic percent (at.%) at 1023 K<sup>42</sup>), whereas Ni is highly miscible with a Mg melt<sup>43</sup>.

The precursor comprised an approximately 150  $\mu\text{m}$ -thick Fe<sub>30</sub>Ni<sub>70</sub> sheet of FCC structure with compositional uniformity, as confirmed by X-ray diffraction and energy-dispersive X-ray spectroscopy (EDX) analyses (see Supplementary Fig. 1). Figure 3a shows cross sections of microstructures formed by immersing the precursor alloy in pure Mg, Mg<sub>95</sub>Ni<sub>5</sub>, Mg<sub>90</sub>Ni<sub>10</sub>, and Mg<sub>85</sub>Ni<sub>15</sub> baths at 1023 K for 30 min. The top row of Fig. 3a shows the low



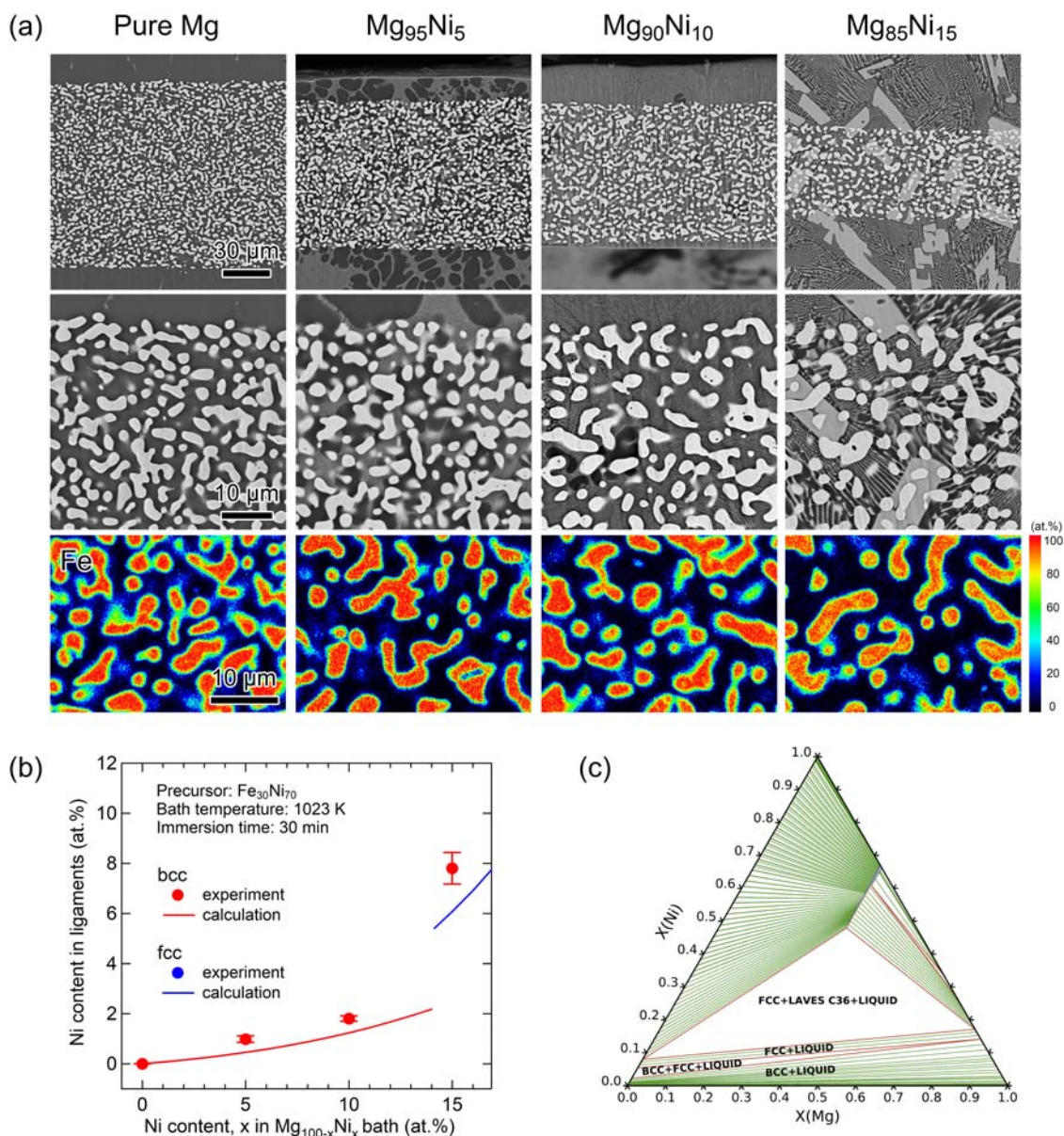


**Fig. 3** Liquid metal dealloying of an Fe-Ni precursor in various Mg-Ni alloy baths. **a** Cross-sectional microstructure and quantitative EDX map of Fe formed by immersing the Fe<sub>30</sub>Ni<sub>70</sub> precursor in pure Mg, Mg<sub>95</sub>Ni<sub>5</sub>, Mg<sub>90</sub>Ni<sub>10</sub>, and Mg<sub>85</sub>Ni<sub>15</sub> baths at 1023 K for 30 min. **b** Relationship between the Ni content in the Mg bath and that in the ligament. Plots and curves represent experimental results and numerical calculation results from the Calphad assessment of the Fe-Ni-Mg system. Red plot indicates BCC structure of ligaments. Red and blue curves indicate calculated equilibrium composition between BCC or FCC ligaments and liquid bath. Each plot represents average composition of ligaments, and the error bars show the standard deviation. **c** Calculated phase diagram of the Fe-Ni-Mg ternary system at 1023 K<sup>40</sup>.

magnification scanning electron microscopy (SEM) images and reveals the whole cross section structures. The middle and bottom rows display high magnification micrographs showing the cross-section of each ligament and their quantitative EDX mapping of Fe in atomic %, respectively. In each bath, the dealloying reaction promotes the formation of interconnected ligaments with widths of a few micrometers. The bath regions featured inhomogeneous microstructures because they had hypo- or hyper-eutectic compositions, and solidified by forming Mg (dark contrast) and Mg<sub>2</sub>Ni phases (bright contrast) during cooling. The quantitative EDX map of Fe content in the ligaments obtained from the bath composition up to 10% of Ni shows that the ligaments were largely composed of Fe ( $\cong 98$  at.%) and contained a small amount of Ni ( $\cong 2$  at.%), and their composition was uniform within the cross section. The average contents of Ni in the ligaments

obtained using the various bath compositions are displayed in Fig. 3b as a function of the Ni content in the bath. It clearly reveals that more Ni is distributed in the liquid phase rather than in the solid ligament phase in this system. The Ni content in the ligaments formed in pure Mg was nearly zero (below the detection limit of EDX), which was consistent with previously reported results<sup>21</sup>. Increasing the Ni content of the bath to 10% led to a slight increase of the Ni content in the ligaments. The crystalline structure of the resulting ligaments was determined by electron backscatter diffraction (EBSD) measurements (see Supplementary Fig. 2a), and is reported in Fig. 3b. For Ni contents below 2%, the ligaments had a body-centered cubic (BCC) structure, which was expected from the solubility of Ni in BCC Fe at the dealloying temperature. For the Mg<sub>85</sub>Ni<sub>15</sub> bath, the residual content of Ni in the ligaments reached 8%, which exceeds

solubility of Ni in BCC Fe but its crystalline structure was determined to be BCC. It is presumably because of phase transformation during cooling down of the sample.

These results can be rationalized by the simple thermodynamic model presented in the previous subsection (see Fig. 2). To go beyond this qualitative approach, we also used a more realistic thermodynamic model based on a Calphad assessment of the Fe-Ni-Mg system<sup>40</sup>. Figure 3c shows the calculated phase diagram for the Fe-Ni-Mg ternary system at the dealloying temperature (1023 K). The tie-lines between the Mg-rich and Fe-rich regions of the phase diagram confirm that an increase in the Ni content of the bath led to a small increase in the Ni content of the ligaments. This relationship between the Ni content of the bath and that of the ligaments is also reported in Fig. 3b with continuous lines that compare well with the experimental results. The discontinuity at approximately 14% Ni in the bath corresponded to the BCC–FCC transition of the Fe-Ni system at this temperature (see the phase diagram Fig. 3c), which closely matched the experimental observations. Therefore, the compositions of the phases resulting from the dealloying process were reproduced by the Calphad calculations, demonstrating that the microstructures obtained from the dealloying reaction were close to thermodynamic equilibrium.

From the top row of Fig. 3a, it is seen that the thickness of the dealloyed samples decreases with increasing the content of Ni in the bath. The thickness reduction is the result of the leakage of immiscible component (Fe) into the bath<sup>37</sup>. In case of the pure Mg bath in which the solubility of Fe is negligibly small, the thickness reduction was small because melt is spontaneously saturated by a small amount of leak of Fe from the sample. However, as the Ni content in the bath increases, the miscibility of Fe in the bath increases allowing more Fe to leak in the bath for saturation. This caused a significant reduction of the thickness of the samples in baths with high content of Ni. These results are similar to those reported by Lai et al. who studied effect of the leak of immiscible element on the topology of dealloyed material<sup>37,38</sup>. They numerically and experimentally analyzed the effect of Ti addition to the Cu bath on the topology of dealloyed structure in the Ta-Ti-Cu system. They predicted that the addition of Ti to Cu bath promotes the leakage of Ta into the bath, preventing the development of a topologically connected structure. This is supported by their experiment showing that using a  $\text{Ti}_{20}\text{Cu}_{80}$  melt resulted in a non-connected microstructure<sup>37</sup>. In the conventional LMD systems mentioned here (Fe-Ni-Mg and Ta-Ti-Cu), even if a significant amount of the miscible element is added to the bath, only a small amount of the miscible element is retained in the ligaments. To make matters worse, it induces significant leakage of immiscible element, prohibiting the formation of a connected structure. Thus, the conventional LMD systems did not enable the PLMD we intended to do.

**Liquid metal dealloying of a Fe-Ni precursor in various Bi-Ni alloy baths.** We investigated the dealloying of Fe-Ni precursors in Bi-based liquid baths. As with Mg, Fe is immiscible in liquid Bi. In addition, the mixing enthalpy between Ni and Bi is positive<sup>44</sup> but the solubility of Ni in liquid Bi remains approximately 20% at 1023 K<sup>45</sup>, promoting the selective dissolution of Ni in the liquid Bi bath, and therefore the dealloying reaction. Such a selection of the bath has not been done in most of previous LMD works<sup>15,19–25,28–31,37</sup> that opted for a bath with negative mixing enthalpy with the miscible element, except for several systems<sup>26,27,33</sup>. Because of the non-negligible solubility of Fe in the Bi melt at this temperature ( $\cong 0.1$  at.%)<sup>45</sup>, we limited the undesired leakage of Fe in the liquid by initially saturating the

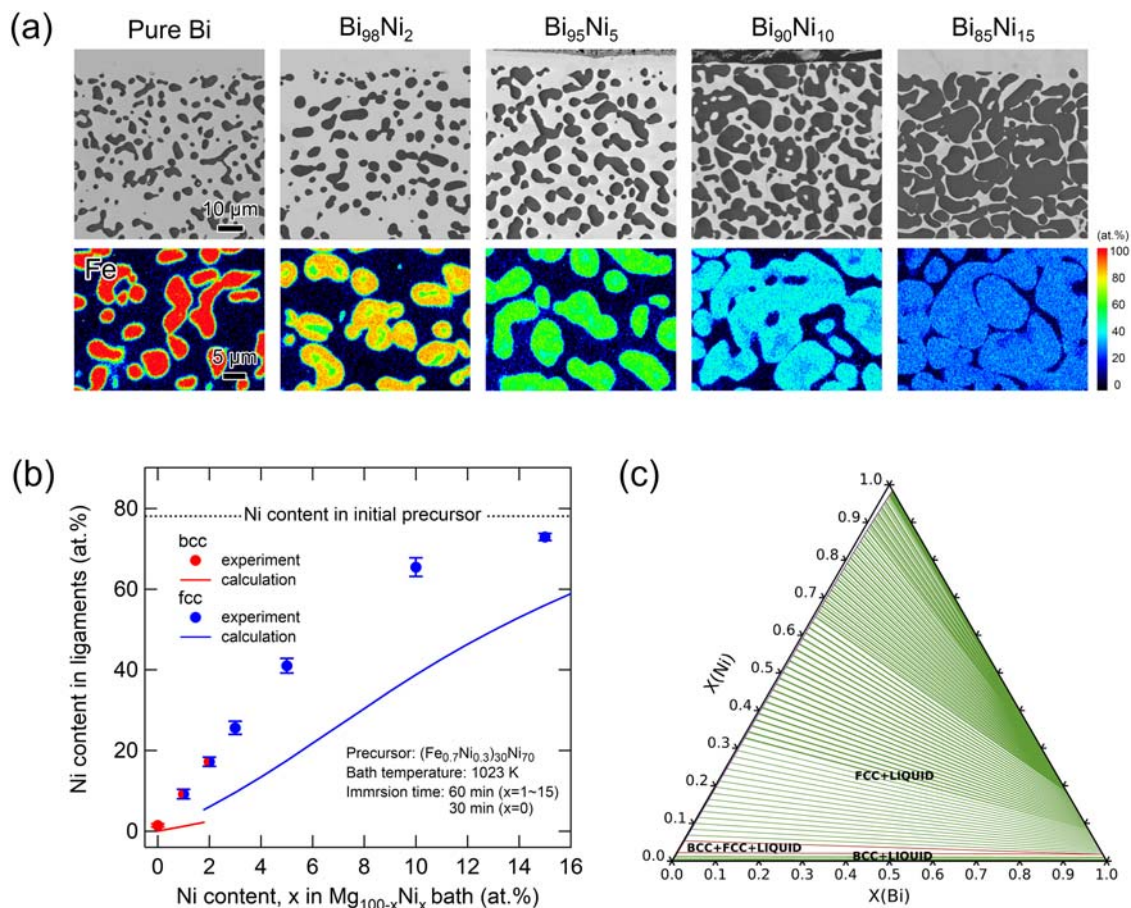
baths by immersing pure Fe in them for 10 min prior to conducting the LMD experiment. A  $(\text{Fe}_{0.7}\text{Ni}_{0.3})_{30}\text{Ni}_{70}$  precursor was prepared (see Supplementary Fig. 1 for details) and immersed in Bi-based baths with various Ni contents.

Figure 4a shows SEM cross sections of the resulting microstructures and quantitative EDX maps for Fe obtained after immersion for 30 and 60 min in the liquid bath. The dark and bright contrasts in the images represent the ligament and bath phases, respectively. Each microstructure had a similar ligament morphology but the volume fraction of the ligaments increased significantly as the Ni content of the bath increased. The average contents of Ni measured near the surface of ligaments derived using the various bath compositions are displayed in Fig. 4b as a function of the Ni content in the bath. The crystalline structure of the resulting ligaments determined by EBSD measurements (see Supplementary Fig. 2b) is also shown on the same graph. Although dealloying in pure Bi still led to the formation of 98% Fe ligaments of BCC structure, the EDX measurements show that increasing the amount of Ni in the liquid bath promoted the formation of FCC ligaments with increasing amounts of residual Ni. It should be noted that when the Ni content of the bath was high, we did not observe complete passivation where the dealloying front stops and the development of a connected morphology is arrested. Dealloying took place primarily at the grain boundaries of the precursor structure, which are regions of fast diffusion. It should also be noted that the EDX maps of the ligaments show compositional heterogeneities: the Ni content at the center of the ligaments remained high, indicating that thermodynamic equilibrium was not entirely reached.

The EBSD analysis presented in Supplementary Fig. 2b also shows that the ligaments were polycrystalline with a fine-grained microstructure at the surface and large grains in the center of the ligaments. These microstructures suggest that the ligament formation mechanism in Bi is different from that in a Mg-based bath. The ligaments at the dealloying front might have contained a high content of Ni because the dissolved Ni develops a diffusion profile in the bath between the dealloying front and the dealloying back. The Ni content in liquid in contact with a ligament continuously decreases over time because Ni diffuses away in the liquid bath. Therefore, the Ni content in the ligaments also decreases progressively over time via solid diffusion mechanism. This is supported by the dealloying front shown in Supplementary Fig. 3b, where ligaments with high Ni content were formed at the dealloying front and the Ni content decreased as the distance from dealloying front increased. Therefore, Ni dissolution occurs more slowly in Bi baths than in Mg baths, and the ligaments do not reach equilibrium even after prolonged immersion (1 h).

To compare these experimental results with numerical predictions, we built a Calphad model of the ternary Fe-Ni-Bi system (see the Methods section for details). Figure 4c shows a ternary phase diagram for the Fe-Ni-Bi system at the dealloying temperature, and the curves in Fig. 4b report the calculated equilibrium between solid Fe-Ni and the Bi-Ni bath. Although calculation result differs significantly from the experimental results, the tendency that Ni content in the solid and liquid phase are completely different from that in Mg bath can be seen. The Ni content in the ligaments is much higher than in the liquid bath, suggesting possibility of a composition control of Ni in the ligament through a small Ni addition in the bath. The discrepancy between experiment and calculation can be attributed to that the dealloying reaction has not reached to the equilibrium state. As shown in Fig. 4a, the dealloying reaction was not finished in some baths in the sense that the composition in the ligaments remains heterogeneous even after 60 min of dealloying.





**Fig. 4** Liquid metal dealloying of an Fe-Ni precursor in various Bi-Ni alloy baths. **a** Cross-sectional microstructures and quantitative EDX maps of Fe measured near the surface of sample, formed by immersing the  $(\text{Fe}_{0.7}\text{Ni}_{0.3})_{30}\text{Ni}_{70}$  precursor in Fe-saturated Bi, Bi<sub>98</sub>Ni<sub>2</sub>, Bi<sub>95</sub>Ni<sub>5</sub>, Bi<sub>90</sub>Ni<sub>10</sub>, and Bi<sub>85</sub>Ni<sub>15</sub> baths at 1023 K. The immersion time was 30 min for the pure Bi bath and 60 min for the other baths. **b** Relationship between the Ni content in the Bi bath and that in the ligament. Red or blue plots indicate BCC or FCC structure of ligaments. Red and blue curves indicate calculated equilibrium composition between BCC or FCC ligaments and liquid bath. Each plot represents the average composition of ligaments, and the error bars show the standard deviation. **c** Calculated phase diagram for the Fe-Ni-Bi ternary system at 1023 K (see “Methods”).

However if these experiments would be carried out longer, composition of the ligaments would converge towards a thermodynamic equilibrium that could be predicted by the phase diagram of the system if it is properly assessed. The discrepancy can also be attributed to the limitations of the Calphad model used for these calculations. The Fe-Ni-Bi model was built by combining databases of the binary systems Fe-Ni<sup>40</sup>, Bi-Fe<sup>45</sup>, and Bi-Ni<sup>41</sup> found in recent literature. In particular, the assessments of the Bi-Ni systems available in the literature<sup>41</sup> are based on experimental measurements of the mixing enthalpy performed for higher temperatures than those characteristics of the LMD experiments presented here. It is also possible that non-negligible ternary interaction terms are important for precisely assessing this system. In all cases, this discrepancy reveals that the thermodynamic model proposed for Fe-Ni-Bi could be improved by studying more precisely the range of compositions and temperatures relevant for the dealloying experiment, and by precisely assessing the full Fe-Ni-Bi ternary system.

**Application of partial liquid metal dealloying to synthesize binary Fe-Ni alloy composite.** We demonstrated in the previous two sections that LMD differs significantly in Mg and Bi baths in terms of the equilibrium composition and dealloying kinetics. We then used a Mg-Bi mixture as a liquid bath, hoping to take

advantage of the rapid dealloying process promoted by Mg and control of the ligament composition facilitated by Bi.

A  $(\text{Fe}_{0.7}\text{Ni}_{0.3})_{30}\text{Ni}_{70}$  precursor was prepared. This composition formula was chosen because we intended to remove 70 at.% Ni from the precursor alloy and retain 30 at.% Ni in the final product. Formation of an interconnected structure from a precursor containing a total 30 at.% of insoluble components and a 70 at.% of soluble components is confirmed by the previous studies<sup>15,21</sup>. The precursor was immersed in various baths of composition  $(\text{Mg}_{0.5}\text{Bi}_{0.5})_{100-x}\text{Ni}_x$  at 1023 K for 30 min. For every Ni content in the bath, a bicontinuous structure formed throughout the sample with a ligament size of the order of 1 μm. For example, Fig. 5a shows the microstructure and EDX mapping obtained after immersion in a bath containing 1.5 at.% Ni. We observed the samples without removing bath component because the Fe-Ni ligaments are susceptible to corrosion and an etching solution to selectively remove the bath component could not be found. However, the SEM micrograph, EDX maps, and EBSD phase map (shown in Supplementary Fig. 2c) on the ligament clearly reveal the interconnected structure, composition and phase of ligaments formed during the LMD experiment. As expected, the EDX composition maps reveal the formation of Fe-Ni ligaments embedded in the Mg-Bi-rich former liquid phase. The resulting content of Ni in the ligaments produced using different amounts of Ni in the bath is reported in Fig. 5b. The

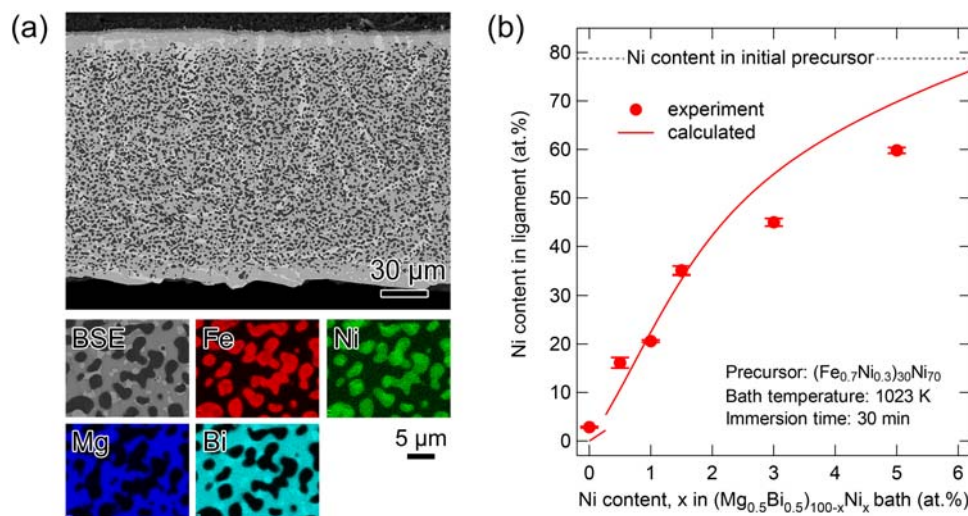


**Fig. 5 Synthesis of composites Fe-Ni binary alloy by partial liquid metal dealloying.** **a** Cross-sectional microstructure and EDX maps of the  $(\text{Fe}_{0.7}\text{Ni}_{0.3})_{30}\text{Ni}_{70}$  precursor immersed in the  $(\text{Mg}_{0.5}\text{Bi}_{0.5})_{98.5}\text{Ni}_{1.5}$  bath at 1023 K for 30 min. **b** Relationship between the Ni content of a ligament and that of the  $(\text{Mg}_{0.5}\text{Bi}_{0.5})_{100-x}\text{Ni}_x$  bath for the immersion of the  $(\text{Fe}_{0.7}\text{Ni}_{0.3})_{30}\text{Ni}_{70}$  precursor at 1023 K for 30 min. The curves indicate the predicted equilibrium composition of the Fe-Ni ligament versus the Ni content of the  $(\text{Mg}_{0.5}\text{Bi}_{0.5})$ -Ni bath, calculated using Thermo-Calc software. Each plot represents the average composition from different areas, and the error bars show the standard deviation.

solid line in Fig. 5b indicates the equilibrium composition of the Fe-Ni ligament versus the Ni content in a  $(\text{Mg}_{0.5}\text{Bi}_{0.5})$ -Ni bath, calculated from a Calphad model of the Fe-Ni-Mg-Bi system (see the Methods section). It closely matches the experimental results, especially at low Ni content. This agreement contrasts with the case of the Bi bath discussed above, and can be explained by the fact that the composition relevant to this LMD experiment (approximately 50 at.% Bi in the bath) had been more carefully assessed experimentally to build the thermodynamic model of the Bi-Ni system. However, the discrepancy between experiment and calculation in the high Ni content region can be attributed to the role of ternary interaction terms that are not included in the present model.

It should be noted that both the experimental and calculated results show that the composition of the ligaments was more sensitive to the Ni content of the bath in the case of the  $(\text{Mg}_{0.5}\text{Bi}_{0.5})$ -based bath than to the Ni content of the Mg and Bi baths; in other words, the curve presented in Fig. 5b has a steeper dependence on Ni content in the bath than in Fig. 4b. This can be rationalized by analyzing the thermodynamic model of the system in more detail; in particular, adding Mg to the Bi bath increased the mixing enthalpy between the bath and Ni, which explains the steeper dependence of Fig. 5b compared to Fig. 4b.

**Application of partial liquid metal dealloying to synthesize multicomponent Ni-containing porous alloys.** The previous subsection indicates that the PLMD could be used to produce porous multicomponent alloys of specific compositions. In this subsection, we describe the use of this strategy for the production of a porous austenitic steel (with target compositions close to the 316 L grade) and porous HEAs with the FCC structure.

**Porous grade 316L austenitic stainless steel.** 316L austenitic stainless steel is characterized by the typical composition  $\text{Fe}_{65.7}\text{Cr}_{19.4}\text{Ni}_{13.4}\text{Mo}_{1.5}$  (in at.%) and is widely used in various fields of modern industry owing to its excellent mechanical properties and high corrosion resistance<sup>46</sup>. This quaternary alloy can be synthesized into a porous metal using a Mg-Bi-based bath. Whereas Mo is highly immiscible in Mg and Bi, Cr is slightly miscible in Bi. Therefore, to avoid the leakage of Cr from the

precursor into the liquid bath, we also added a small amount of Cr to the bath. In particular, we found that a  $(\text{Mg}_{0.75}\text{Bi}_{0.25})_{92}\text{Ni}_7\text{Cr}_1$  bath equilibrated with the target composition of the grade 316 L stainless steel. Figure 6a shows cross-sections of the microstructures obtained after immersing a  $(\text{Fe}_{0.657}\text{Cr}_{0.194}\text{Ni}_{0.134}\text{Mo}_{0.015})_{30}\text{Ni}_{70}$  sheet in this bath at 1023 K for 10 min. It shows that the dealloying reaction reached the center of the precursor samples and resulted in the formation of sub-micrometer ligaments. The image analysis on the cross section, shown in Supplementary Fig. 5a, reveals that the average ligament cross section size was 518 nm. After etching this composite material, we obtained a bulk plate-shaped porous metal, as shown in Fig. 6b, c. To investigate elemental distribution within the ligaments, an epoxy resin was infiltrated into the porous sample and ligament cross section was made by ion beam polishing. The EDX composition maps acquired from the ligament cross-sections indicate the uniform distribution of Fe, Cr, Ni, and Mo in the ligaments as shown in Fig. 6d. The average composition of the porous metal was  $\text{Fe}_{64.9}\text{Cr}_{20.1}\text{Ni}_{13.6}\text{Mo}_{1.4}$  (in at.%), showing excellent agreement with the composition range of grade 316L stainless steels. The results of X-ray diffraction analysis shown in Fig. 6e confirm the FCC structure of the porous samples. Therefore, we successfully used the PLMD to produce a porous austenitic stainless steel with a composition close to that of grade 316 L stainless steel.

**Porous high-entropy FCC alloy.** PLMD can also be applied to produce HEAs with FCC structures, thanks to the austenite-stabilizing properties of Ni. HEAs are generally defined as alloys composed of multiple elements mixed in high (often equiatomic) concentration<sup>47</sup>, and we aimed at a target FCC alloy with the composition  $\text{V}_{15}\text{Cr}_{15}\text{Fe}_{20}\text{Co}_{25}\text{Ni}_{25}$  (in at.%) (see Supplementary Fig. 4). Components V and Co are strongly immiscible in Mg and Bi, whereas Cr is slightly miscible in Bi. It is therefore necessary to adjust the Cr content of the bath to prevent Cr leakage from the solid ligaments. Various  $(\text{Mg}_{0.5}\text{Bi}_{0.5})_{100-x-y}\text{Ni}_x\text{Cr}_y$  baths were investigated and the  $(\text{Mg}_{0.5}\text{Bi}_{0.5})_{98.2}\text{Ni}_{1.5}\text{Cr}_{0.3}$  bath was found to equilibrate with a solid phase close to the target composition. Figure 7a shows whole cross-sectional image and Fig. 7b shows ligaments morphology at high magnification for the



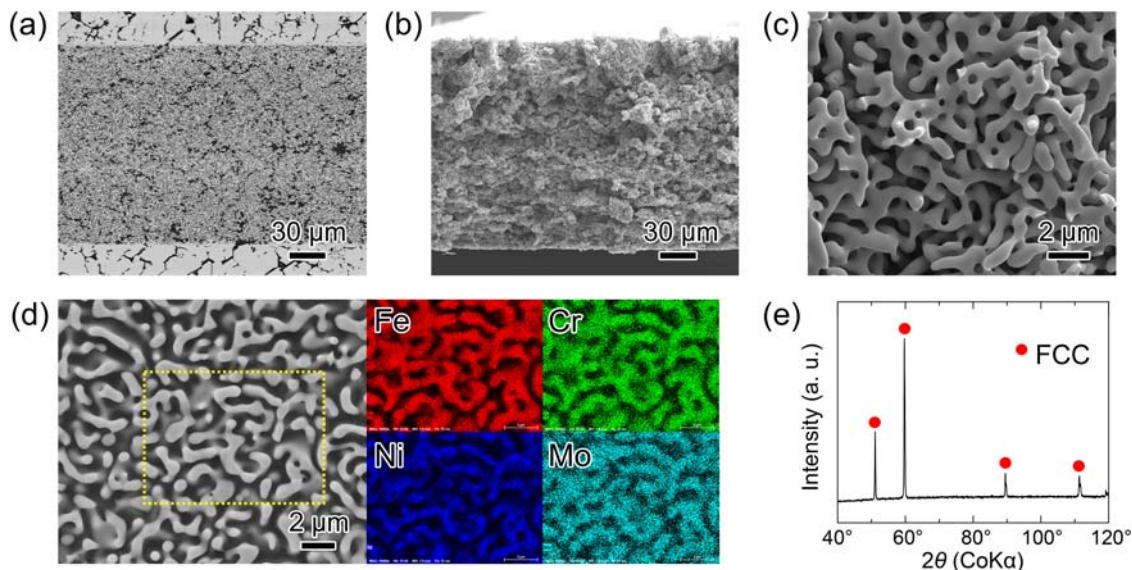


**Fig. 6 Synthesis of a porous grade 316 L austenitic stainless steel by partial liquid metal dealloying.** **a** Cross-sectional microstructure of an  $(\text{Fe}_{0.657}\text{Cr}_{0.194}\text{Ni}_{0.134}\text{Mo}_{0.015})_{30}\text{Ni}_{70}$  sheet precursor immersed in an  $(\text{Mg}_{0.75}\text{Bi}_{0.25})_{92}\text{Ni}_7\text{Cr}_1$  bath at 1023 K for 10 min, and **b**, **c** the same sample after etching in a bath containing an aqueous solution of nitric acid. **d** Cross-section of the porous sample and the EDX maps for Fe, Cr, Ni, and Mo acquired from the region indicated by the yellow square. The porous plate sample was embedded in an epoxy resin to produce a flat cross section of ligaments by ion-milling. **e** X-ray diffraction pattern obtained from the lateral surface of the porous sample shown in **b**.

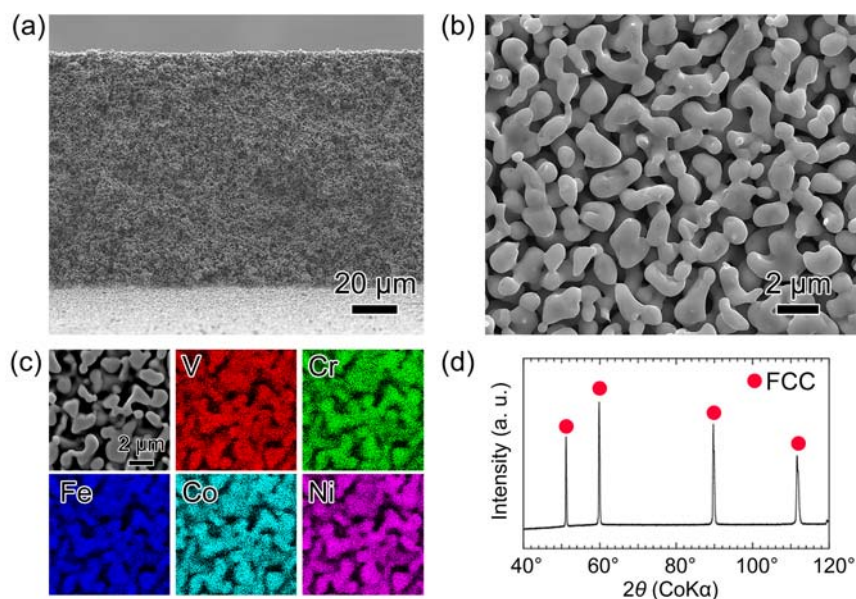


**Fig. 7 Synthesis of a porous high-entropy FCC alloy by partial liquid metal dealloying.** Scanning electron microscopy (SEM) images for **a** whole cross-section at low magnification and **b** ligament morphology at high magnification, and **c** energy-dispersive X-ray spectroscopy (EDX) maps of V, Cr, Fe, Co, Ni obtained from the  $(\text{V}_{0.15}\text{Cr}_{0.15}\text{Fe}_{0.20}\text{Co}_{0.25}\text{Ni}_{0.25})_{50}\text{Ni}_{50}$  precursor after immersion in an  $(\text{Mg}_{0.5}\text{Bi}_{0.5})_{98.2}\text{Ni}_{1.5}\text{Cr}_{0.3}$  bath for 30 min at 1023 K, followed by etching with nitric acid solution to remove bath components. Note that the EDX maps were acquired from the cross section of ligaments of porous sample. **d** X-ray diffraction pattern obtained from the lateral surface of the porous sample shown in **a**.

$(\text{V}_{0.15}\text{Cr}_{0.15}\text{Fe}_{0.20}\text{Co}_{0.25}\text{Ni}_{0.25})_{50}\text{Ni}_{50}$  precursor alloy after immersion in this liquid for 30 min at 1023 K, followed by etching in nitric acid to remove bath components. They reveal an interconnected porous structure spreading over the sample. The average ligament cross section size was determined to be 753 nm (Supplementary Fig. 5b). Figure 7c shows the EDX composition maps acquired from the cross section of ligaments in the porous sample, which reveals uniform distribution of the desired elements. The composition of the ligaments was  $\text{V}_{14.9}\text{Cr}_{11.9}\text{Fe}_{18.8}\text{Co}_{21.3}\text{Ni}_{33.2}$ , i.e., close to the target composition. These ligaments

had a FCC structure, as demonstrated by the X-ray diffraction spectrum shown in Fig. 7d. Therefore, we demonstrated that the austenite-stabilizing properties of Ni facilitate the use of the PLMD to produce porous HEAs with FCC structures.

## Discussion

We successfully fabricated Ni-containing porous and composite alloys by partially dealloying Ni from precursor alloys, and demonstrated that adding Ni to the liquid metal enables control of the residual Ni content of the ligaments, provided that the



liquid metal is chosen adequately. The dealloying reaction naturally ceases when the composition of the solid ligaments reaches a thermodynamic equilibrium with the melt. A simple thermodynamic model enabled us to rationalize these findings. We also performed Calphad calculations and compared quantitatively the results with those obtained experimentally.

Adding Ni to the liquid bath also reduces the thermodynamic driving force that promotes the dealloying reaction. Lai et al. demonstrated theoretically that, above a threshold amount, the addition of miscible element (B) to the liquid bath can lead to a planar dissolution regime because the critical driving force for interfacial spinodal decomposition is not reached<sup>38</sup>. We did not observe planar dissolution in our experiments; even with large amounts of Ni in the Bi bath, the dealloying reaction was always facilitated by the presence of grain boundaries owing to the enhanced diffusivity. However, when the composition of the bath was in equilibrium with that of the precursor alloy, i.e. approaching the dashed lines in Figs. 4b and 5b, no dealloying reaction occurred because under those circumstances, there was no driving force for the dissolution of Ni in the bath.

We would like to highlight the difference and advances of our work with respect to related previous studies. In ref. <sup>37</sup>, Lai et al. studied the dealloying of Ta-Ti (=A-B) alloy in a Ti-Cu (=B-C) bath, which is technically similar to our experiments. In their work, they opted for a bath that has a negative interaction parameter between B and C, which is also the case of Fe-Ni-Mg. In such systems, the negative mixing enthalpy between B and C component promotes the dissolution of B in the liquid metal C, even if the C melt contains some amount of B. In this case, we must add a large amount of B in the bath to preserve desired content of B in the ligament (see Fig. 3b), however, the large amount of B in the melt inevitably causes a significant leakage of A and lead to the formation of non-connected structures<sup>37</sup>. Lai et al. demonstrated numerically and experimentally that adding Ag to the Cu melt enables to reduce the solubility of Ta in the Ti-Cu melt and therefore limit the leakage of Ta into the melt, retarding the pinch-off of ligament and thereby promoting the formation of connected topologies.

On the contrary, the Bi-based bath used in our work is characterized by a positive interaction parameter between B and C. In such a case, the positive mixing enthalpy between the bath and the B component makes the dissolution of B in the liquid C more difficult, such that a large amount of B can be retained in solid ligament. Because of this, only a few atomic percent of B element in the bath is sufficient to preserve several ten atomic percent of B in the ligaments (see Figs. 4b and 5b), which also prevents the leakage of immiscible A component in the bath. Choosing the appropriate composition of the precursor is also important for the formation of interconnected structure in the PLMD. Previously, the precursor composition in LMD experiments was considered based on the formula of  $A_{1-x}B_x$ . In the PLMD, this composition formula is no longer useful because there are two types of B element; one is to remain in solid ligaments ( $B^{\text{insoluble}}$ ) and the other is to dissolve in the bath ( $B^{\text{soluble}}$ ). For a target ligament composition,  $A_{1-x}B_x$ , one should distinguish two types of B and consider composition formula,  $(A_{1-x}B_x^{\text{insoluble}})_{1-z}B_z^{\text{soluble}}$  such that the value of  $z$  falls into the range forming interconnected structures as demonstrated here.

The concept of PLMD presented in this work therefore goes beyond the work presented in ref. <sup>37</sup> by showing how the choice of the melt enables to control the composition of the resulting microstructure while conserving connected microstructures.

Furthermore, it is possible to draw an analogy between the partial liquid metal dealloying technique developed herein and the partial dealloying of Ag in electrochemical dealloying experiments of Ag-Au alloys<sup>48,49</sup>. It has been demonstrated that tuning the applied potential during electrochemical dealloying experiments

enables control of the amount of Ag remaining in the ligaments. Therefore, a comparison can be made between the role of the applied potential in electrochemical dealloying and the composition of the liquid bath in LMD, because both of them control the driving force that promotes the dealloying reaction. However, the choice of the liquid composition in LMD appears more versatile than the choice of the applied potential in electrochemical dealloying, which is necessarily the same for all elements. As performed in the present work, the composition of the liquid bath can be tuned by adding several elements in various quantities to control the partial dealloying of different components, thereby tailoring the composition of the resulting microstructure.

The present work also demonstrates that Calphad method is a promising tool for guiding liquid metal dealloying experiments. This has not been considered before because the development of connected morphologies in LMD was initially regarded as a non-equilibrium process<sup>19</sup>. However, the resulting morphologies are characterized by small dimensions and large surface areas that promote rapid convergence to a thermodynamic equilibrium by means of liquid, solid, and interfacial diffusion mechanisms. Although the time-scales of LMD experiments are generally shorter than those in the thermodynamic assessment of metallic systems, assuming thermodynamic equilibrium may be considered as a first approximation for predicting the resulting concentrations in both solid and liquid phases. As revealed in the present work, these predictions are as good as the thermodynamic assessment of the system. In particular, the discrepancy between the numerical and experimental results observed in the Bi bath revealed the weaknesses of the thermodynamic assessment of the Fe-Ni-Bi system. We believe that LMD experiments can also be viewed as high-throughput methods that enable the collection of data on metal systems, including element couples characterized by large mixing enthalpies. Such systems have attracted little attention because they are considered irrelevant to alloy design.

Finally, we should point out that the concept of PLMD presents possibilities for the production of porous alloys with improved mechanical and functional properties. In this work, Fe-Ni-based systems were chosen because they form a solid solution in a wide composition and temperature range. We used this system to demonstrate feasibility and versatility of the PLMD concept. However, the PLMD can be applied to specific materials to optimize compositions in order to achieve high mechanical and catalytic performances. First, Ni-containing alloys exhibit excellent mechanical properties at both low (cryogenic applications of 316L steels) and high temperatures (Ni-based superalloys used for turbine blades in aircraft engines), which are the result of solid solution and precipitate strengthening. Harnessing these strengthening mechanisms could improve the mechanical properties of nanoporous materials, thereby compensating for their intrinsic mechanical weaknesses<sup>50</sup>. HEAs such as the one elaborated in this work also present promising catalytic properties for a variety of reactions<sup>51</sup>. This can be attributed to the large variety of active sites found at the surfaces of such alloys. Together with a recent study that focused on HEAs with BCC structures<sup>28</sup>, the present work demonstrates that LMD can be used to produce porous HEAs with targeted compositions. Such porous HEAs are freestanding materials with large specific surface areas and both positive and negative surface curvatures, which are attractive properties for catalytic applications. Therefore, we believe that the recent development of HEAs as catalytic materials will benefit greatly from the liquid metal dealloying technique, and more particularly from the PLMD strategy introduced in the present work.

## Methods

**Precursor preparation.** The precursor alloys were prepared by arc-melting using pure Fe (99.99 mass%, Toho Zinc Co., Ltd, Japan), Cr (99.9 mass%, Kojundo

Chemical Lab. Co., Ltd., Japan), Ni (99.99 mass % Furuuchi Chemical Co., Ltd., Japan), V (99.9 mass%, Taiyo Koko Co., Ltd., Japan), and Co (99.99% Japan Metals & Chemicals Co., Ltd., Japan) under a high-purity Ar gas atmosphere. The precursor ingots were cold-rolled into plates of approximately 200  $\mu\text{m}$  thickness.

**Liquid metal dealloying.** Pure Mg (99.9 mass% Fuji Light Metal Co., Ltd., Japan), Bi (99.99 mass% Mitsuwa Chemical Co., Ltd., Japan), and the additive elements (Ni and/or Cr) at the designated molar ratio were placed in a cylindrical graphite crucible (34 mm in diameter; 40 mm in height). The crucible was placed into the heating coil of the induction furnace. The typical volumes of the precursor and bath were 0.02 and 18  $\text{cm}^3$ , respectively. The precursor plate, which had been spot welded to the pure Fe wire, was connected to the arm inside the induction furnace. The furnace chamber was once vacuumed to  $10^{-3}$  Pa and filled by Ar gas of ambient pressure. Then the crucible was inductively heated and held for about 30 min to make a bath homogeneous temperature and composition. Bath temperature was monitored by a K-type thermocouple inserted into the hole on the crucible wall. The precursor was immersed into the bath by operating the arm and held for designated time. After immersion, the sample was taken out from the bath and cooled to room temperature about 300 K.

**Porous metal extraction.** To extract the porous metal, the sample were immersed in an aqueous solution of nitric acid to remove the bath component. During this acid treatment, the bath component was etched away, whereas the porous metals containing Cr were passivated and preserved in their three-dimensional morphology.

**Sample analyses.** The phase of the sample was identified using an X-ray diffractometer with a Co tube (Bruker D8 Advance). The microstructure and the composition were investigated using a scanning electron microscope (SEM, Carl Zeiss Ultra 55) equipped with an energy-dispersive X-ray spectrometer (EDX, Bruker X-flash). The phase of ligaments in the composite samples was analyzed by electron backscatter diffraction (EBSD; JSM-7100F), and orientation imaging microscopy (OIM) software (version 7.0). The flat cross section for electron microscope observation was prepared by Ar ion milling (JEOL IB-19530CP).

**Thermodynamics calculations.** The predictions of ligament compositions reported in Figs. 3–5 were obtained from thermodynamics calculations using Thermo-Calc software. We first built a thermodynamic database pertaining to the elements Fe, Ni, Bi, and Mg. Because of the strong immiscibility of Mg and Bi in Fe, such systems have not attracted much attention from the alloy-designing community, and no complete assessment of this quaternary system has been proposed in the literature. We started with the thermodynamic assessment of Fe-Mg-Ni performed by Wang et al.<sup>40</sup>, which accurately reproduced the thermodynamics of binary Fe-Mg, Fe-Ni, and Mg-Ni systems as well as some features of the ternary system. To incorporate Bi into this database, we used the thermodynamic assessments of the binary systems Bi-Mg, Bi-Fe, and Bi-Ni that are available in the literature<sup>41,45,52,53</sup>. Therefore, the database represented the binary interactions well but did not include ternary interaction terms. It should be noted that the Bi-Ni assessment used herein<sup>41</sup> relies on experimental data obtained for temperatures higher than the temperature of the dealloying experiments, which explains the discrepancy between the numerical and experimental results for the Fe-Ni-Bi system. The numerical results presented as continuous lines in Figs. 3–5 were obtained within the infinite bath limit: we assumed that the liquid bath was sufficiently large so that the dissolution of Ni did not significantly change its composition. We used Thermo-Calc software to determine the contents of the solid ligaments that were in equilibrium with the various Ni contents of the liquid baths. In other words, we looked for the solid/liquid tie-line that satisfied a prescribed Ni composition of the liquid. For the quaternary case, we imposed the equality of Bi and Mg contents as an extra constraint.

### Data availability

The raw data generated in this study are available at Zenodo.org (<https://doi.org/10.5281/zenodo.7928545>).

### Code availability

The code for obtaining the results of this work is available from the corresponding author on reasonable request.

Received: 18 January 2023; Accepted: 25 May 2023;

Published online: 05 June 2023

### References

1. Editors Wittstock, A., Biener, J., Erlebacher, J. & Bäumer, M. *Nanoporous Gold: From an Ancient Technology to a High-Tech Material* (RSC, 2012).
2. Erlebacher, J. & Seshadri, R. Hard materials with tunable porosity. *MRS Bull.* **34**, 561–568 (2009).
3. McCue, I., Benn, E., Gaskey, B. & Erlebacher, J. Dealloying and dealloyed materials. *Annu. Rev. Mater. Res.* **46**, 263–286 (2016).
4. Ding, Y. & Chen, M. Nanoporous metals for catalytic and optical applications. *MRS Bull.* **34**, 569–576 (2009).
5. Wittstock, A., Zielasek, V., Biener, J., Friend, C. M. & Bäumer, M. Nanoporous gold catalysts for selective gas-phase oxidative coupling of methanol at low temperature. *Science* **327**, 319–322 (2010).
6. Liu, Z. et al. Electrochemical sensor for detection of p-nitrophenol based on nanoporous gold. *Electrochem. Commun.* **11**, 1365–1368 (2009).
7. Chen, L. Y., Yu, J. S., Fujita, T. & Chen, M. W. Nanoporous copper with tunable nanoporosity for SERS applications. *Adv. Funct. Mater.* **19**, 1221–1226 (2009).
8. Pickering, H. W. & Wagner, C. Electrolytic dissolution of binary alloys containing a noble metal. *J. Electrochem. Soc.* **114**, 698–706 (1967).
9. Forty, A. J. Corrosion Micromorphology of noble metal alloys and depletion gilding. *Nature* **282**, 597–598 (1979).
10. Erlebacher, J., Aziz, M. J., Karma, A., Dimitrov, N. & Sieradzki, K. Evolution of nanoporosity in dealloying. *Nature* **410**, 450–453 (2001).
11. Pugh, D. V., Dursun, A. & Corcoran, S. G. Electrochemical and morphological characterization of Pt-Cu dealloying. *J. Electrochem. Soc.* **152**, B455–B459 (2005).
12. Min, U. S. & Li, J. C. M. The Microstructure and dealloying kinetics of a Cu-Mn alloy. *J. Mater. Res.* **9**, 2878–2883 (1994).
13. Han, S. Y. et al. Porous metals from chemical dealloying for solid-state battery anodes. *Chem. Mater.* **32**, 2461–2469 (2020).
14. Liu, X. et al. Formation of three-dimensional bicontinuous structures via molten salt dealloying studied in real-time by in situ synchrotron X-ray nanotomography. *Nat. Commun.* **12**, 3441 (2021).
15. Wada, T., Yubuta, K., Inoue, A. & Kato, H. Dealloying by metallic melt. *Mater. Lett.* **65**, 1076–1078 (2011).
16. Wada, T., Yubuta, K. & Kato, H. Evolution of a bicontinuous nanostructure via a solid-state interfacial dealloying reaction. *Scripta Mater.* **118**, 33–36 (2016).
17. McCue, I. & Demkowicz, M. J. Alloy design criteria for solid metal dealloying of thin films. *JOM.* **69**, 2199–2205 (2017).
18. Lu, Z. et al. Three-dimensional bicontinuous nanoporous materials by vapor phase dealloying. *Nat. Commun.* **9**, 276 (2018).
19. Geslin, P. A., McCue, I., Gaskey, B., Erlebacher, J. & Karma, A. Topology-generating interfacial pattern formation during liquid metal dealloying. *Nat. Commun.* **6**, 8887 (2015).
20. Wada, T., Setyawan, A. D., Yubuta, K. & Kato, H. Nano- to submicro-porous  $\beta$ -Ti alloy prepared from dealloying in a metallic melt. *Scripta Mater.* **65**, 532–535 (2011).
21. Wada, T. & Kato, H. Three-dimensional open-cell macroporous iron, chromium and ferritic stainless steel. *Scripta Mater.* **68**, 723–726 (2013).
22. Kim, J. W. et al. Optimizing niobium dealloying with metallic melt to fabricate porous structure for electrolytic capacitors. *Acta Mater.* **84**, 497–505 (2015).
23. Song, R. et al. Ultrafine nanoporous intermetallic catalysts by high-temperature liquid metal dealloying for electrochemical hydrogen production. *Nat. Commun.* **13**, 5157 (2022).
24. McCue, I. et al. Size effects in the mechanical properties of bulk bicontinuous Ta/Cu nanocomposites made by liquid metal dealloying. *Adv. Eng. Mater.* **18**, 46–50 (2016).
25. Wada, T. et al. Bulk-nanoporous-silicon negative electrode with extremely high cyclability for lithium-ion batteries prepared using a top-down process. *Nano Lett.* **14**, 4505–4510 (2014).
26. Yu, S. G., Yubuta, K., Wada, T. & Kato, H. Three-dimensional bicontinuous porous graphite generated in low temperature metallic liquid. *Carbon* **96**, 403–410 (2016).
27. Greenidge, G. & Erlebacher, J. Porous graphite fabricated by liquid metal dealloying of silicon carbide. *Carbon* **165**, 45–54 (2020).
28. Joo, S. H. et al. Beating thermal coarsening in nanoporous materials via high-entropy design. *Adv. Mater.* **32**, 1906160 (2020).
29. Jeong, Y. B. et al. Beyond strength-ductility trade-off: 3D interconnected heterostructured composites by liquid metal dealloying. *Compos. Part B Eng.* **225**, 109266 (2021).
30. Joo, S. H. & Kato, H. 3D interconnected nanoporous FeCo soft magnetic materials synthesized by liquid metal dealloying. *J. Alloys Compds.* **908**, 164688 (2022).
31. Chuang, A., Baris, J., Ott, C., McCue, I. & Erlebacher, J. A powder metallurgy approach to liquid metal dealloying with applications in additive manufacturing. *Acta Mater.* **238**, 118213 (2022).
32. McCue, I., Karma, A. & Erlebacher, J. Pattern formation during electrochemical and liquid metal dealloying. *MRS Bull.* **43**, 27–34 (2018).
33. Mokhtari, M. et al. Cold-rolling influence on microstructure and mechanical properties of NiCr-Ag composites and porous NiCr obtained by liquid metal dealloying. *J. Alloys Compds.* **707**, 251–256 (2017).
34. Jani, J. M., Leary, M., Subic, A. & Gibson, M. A. A review of shape memory alloy research, applications and opportunities. *Mater. Des.* **56**, 1078–1113 (2014).

35. Adkins, H. & Billica, H. R. The preparation of Raney nickel catalysts and their use under conditions comparable with those for platinum and palladium catalysts. *J. Am. Chem. Soc.* **70**, 695–698 (1948).
36. Wu, H. et al. Ni-based catalysts for low temperature methane steam reforming: recent results on Ni-Au and comparison with other bi-metallic systems. *Catalysts* **3**, 563–583 (2013).
37. Lai, L., Gaskey, B., Chuang, A., Erlebacher, J. & Karma, A. Topological control of liquid-metal-dealloyed structures. *Nat. Commun.* **13**, 2918 (2022).
38. Lai, L., Geslin, P.-A. & Karma, A. Microstructural pattern formation during liquid metal dealloying: phase-field simulations and theoretical analyses. *Phys. Rev. Mater.* **6**, 093803 (2022).
39. Dantzig, J. A. & Rappaz, M. *Solidification, Engineering Sciences* (EPFL Press, 2009).
40. Wang, P. et al. Experimental investigation and thermodynamic calculation of the Fe–Mg–Mn and Fe–Mg–Ni systems. *Int. J. Mater. Res.* **102**, 6–16 (2011).
41. Gierlotka, W., Lee, J., Lim, V., Gąsiorc, W. & Dębski, A. On the Bi–Ni system. Ab initio calculations and thermodynamic remodeling. *Calphad* **69**, 101750 (2020).
42. Nayeb-Hashemi, A. A., Clark, J. B. & Swartzendruber, L. J. The Fe–Mg (iron-magnesium) system. *Bull. Alloy Phase Diagr.* **6**, 235–238 (1985).
43. Nayeb-Hashemi, A. A. & Clark, J. B. The Mg–Ni (magnesium-nickel) system. *Bull. Alloy Phase Diagr.* **6**, 238–244 (1985).
44. Takeuchi, A. & Inoue, A. Classification of bulk metallic glasses by atomic size difference, heat of mixing and period of constituent elements and its application to characterization of the main alloying element. *Mater. Trans.* **46**, 2817–2829 (2005).
45. Boa, D., Hassam, S., Kra, G., Kotchi, K. P. & Rogez, J. The ternary bismuth–iron–antimony system: experimental phase diagram study and thermodynamic evaluation. *Calphad* **32**, 227–239 (2008).
46. Lo, K. H., Shek, C. H. & Lai, J. K. L. Recent developments in stainless steels. *Mater. Sci. Eng. R Rep.* **65**, 39–104 (2009).
47. George, E. P., Raabe, D. & Ritchie, R. O. High-entropy alloys. *Nat. Rev. Mater.* **4**, 515–534 (2019).
48. Qi, Z. & Weissmüller, J. Hierarchical nested-network nanostructure by dealloying. *ACS Nano* **7**, 5948–5954 (2013).
49. Shi, S., Li, Y., Ngo-Dinh, B.-N., Markmann, J. & Weissmüller, J. Scaling behavior of stiffness and strength of hierarchical network nanomaterials. *Science* **371**, 1026–1033 (2021).
50. Weissmüller, J., Newman, R. C., Jin, H.-J., Hodge, A. M. & Kysar, J. W. Nanoporous metals by alloy corrosion: formation and mechanical properties. *MRS Bull.* **34**, 577–586 (2009).
51. Xin, Y. et al. High-entropy alloys as a platform for catalysis: progress, challenges, and opportunities. *ACS Catal.* **10**, 11280–11306 (2020).
52. Niu, C., Li, C., Du, Z., Guo, C. & Chen, S. A thermodynamic assessment of the Bi–Mg–Sn ternary system. *Calphad* **39**, 37–46 (2012).
53. Niu, C., Li, C., Du, Z., Guo, C. & Jing, Y. Thermodynamic assessment of the Bi–Mg binary system. *Acta Metall. Sin. (Engl. Lett.)* **25**, 19–28 (2012).

## Acknowledgements

This work was supported by a Grant-in-Aid for Scientific Research from the Japan Society for the Promotion of Science (JSPS) KAKENHI (grant numbers 20K05126 and 21H04611), and a Grant-in-Aid for Scientific Research on Innovative Areas titled

“Science of New-Class of Materials Based on Elemental Multiplicity and Heterogeneity” (grant number 18H05452) from the Ministry of Education, Culture, Sports, Science, and Technology (MEXT, Japan). P.-A.G. wishes to thank Prof. Peisheng Wang (Central South University, Changsha, China) for providing the parameter file for the Fe–Ni–Mg system, and Prof. Olivier Dezellus (Université Lyon 1, France) for his invaluable help in subduing the Thermo-Calc software. P.-A.G. also wishes to thank the JSPS for supporting his stay in Japan as an International Research Fellow of Japan Society for the Promotion of Science (Invitational Fellowships for Research in Japan (Long-term)). We thank Frank Kitching, MSc., from Edanz (<https://jp.edanz.com/ac>) for editing a draft of this manuscript.

## Author contributions

T.W., P.-A.G., and H.K. developed the concept of the partial liquid metal dealloying, and T.W. designed and performed the experiments. P.-A.G. performed the thermodynamic calculations. D.W. performed the EBSD analyses. T.W. and P.-A.G. wrote the manuscript. All the authors discussed the results and commented on the manuscript.

## Competing interests

The authors declare no competing interests.

## Additional information

**Supplementary information** The online version contains supplementary material available at <https://doi.org/10.1038/s43246-023-00374-3>.

**Correspondence** and requests for materials should be addressed to Takeshi Wada.

**Peer review information** *Communications Materials* thanks the anonymous reviewers for their contribution to the peer review of this work. Primary handling editors: Jet-Sing Lee, John Plummer. A peer review file is available

**Reprints and permission information** is available at <http://www.nature.com/reprints>

**Publisher's note** Springer Nature remains neutral with regard to jurisdictional claims in published maps and institutional affiliations.



**Open Access** This article is licensed under a Creative Commons Attribution 4.0 International License, which permits use, sharing, adaptation, distribution and reproduction in any medium or format, as long as you give appropriate credit to the original author(s) and the source, provide a link to the Creative Commons license, and indicate if changes were made. The images or other third party material in this article are included in the article's Creative Commons license, unless indicated otherwise in a credit line to the material. If material is not included in the article's Creative Commons license and your intended use is not permitted by statutory regulation or exceeds the permitted use, you will need to obtain permission directly from the copyright holder. To view a copy of this license, visit <http://creativecommons.org/licenses/by/4.0/>.

© The Author(s) 2023